Study on the Seepage and Heat Transfer Characteristic of Single Rough Fracture and Intersecting Fracture in Hot-Dry Rock

Wenyu Lv[1], Xinrui Gao[1,*], Li'an Tang[2], Yongping Wu[1], Panshi Xie[1] and Chao Lyu[1,*]

[1] College of Energy and Mining Engineering, Xi'an University of Science and Technology, Xi'an, 710054, China

[2] China Coal Technology Engineering Group Chongqing Research Institute, Chongqing, 400039, China

Revista Internacional
Métodos numéricos
para cálculo y diseño en ingeniería

RIMNI

UNIVERSITAT POLITÈCNICA
DE CATALUNYA
BARCELONATECH

In cooperation with
CIMNE

INFORMATION

Keywords:
Fluid flow
heat transfer
fracture model
numerical simulation
mid-plane fracture

DOI: 10.23967/j.rimni.2025.10.73260

SCIPEDIA Revista Internacional de Métodos Numéricos para Cálculo y Diseño en Ingeniería

Study on the Seepage and Heat Transfer Characteristic of Single Rough Fracture and Intersecting Fracture in Hot-Dry Rock

Wenyu Lv[1], **Xinrui Gao**[1,*], **Li'an Tang**[2], **Yongping Wu**[1], **Panshi Xie**[1] **and Chao Lyu**[1,*]

[1]College of Energy and Mining Engineering, Xi'an University of Science and Technology, Xi'an, 710054, China

[2]China Coal Technology Engineering Group Chongqing Research Institute, Chongqing, 400039, China

---

ABSTRACT

The efficient extraction of geothermal energy from fractured hot dry rock reservoirs requires accurate prediction of subsurface thermo-hydrodynamic processes. In this study, a novel simplified mid-plane fracture model was developed and validated as an approach that bridges the computational efficiency of two-dimensional approximations with the physical accuracy of fully three-dimensional simulations. Three distinct fracture representations were systematically compared: full 3D models, simplified 2D plane fractures, and the proposed rough mid-plane fractures. Discrepancies in flow dynamics and heat transfer predictions were quantified using coupled steady-state and transient numerical simulations. The influence of "X"-type and "V"-type fracture intersections on thermo-hydrodynamic processes was further examined. The results show that the rough mid-plane model accurately captures permeability and flow channeling effects inherent in realistic 3D fracture geometries, outperforming traditional plane approximations. Flow fields and velocity distributions are substantially modified by surface roughness, directly governing heat exchange efficiency. Flow and temperature fields are shown to be dramatically redistributed by variations in fracture aperture and intersection geometry, with heat extraction significantly enhanced by optimal aperture and injection rate combinations. Notably, "X"-type intersections are found to exhibit 40%–60% greater effective heat conduction areas than "V"-type configurations, highlighting their preferential heat transfer characteristics. These findings provide critical insights for the optimization of HDR reservoir performance, contributing to improved strategies for efficient geothermal energy extraction.

OPEN ACCESS

Received: 14/09/2025

Accepted: 21/10/2025

Published: 29/05/2026

DOI
10.23967/j.rimni.2025.10.73260

Keywords:
Fluid flow
heat transfer
fracture model
numerical simulation
mid-plane fracture

1 Introduction

Under the guidance of the "Dual Carbon" goals, China's energy structure is undergoing a rapid transformation, with a notable acceleration in the development of renewable energy sources such as

---

*Correspondence: Xinrui Gao, Chao Lyu (23203077038@stu.xust.edu.cn, lvchao@cumt.edu.cn).

wind, nuclear, solar, and geothermal energy. Among renewable energy sources, geothermal energy is favored because of its wide distribution, extensive reserves, lack of pollution, and high stability [1–3]. Enhanced Geothermal System (EGS) is one of the key technologies for the utilization of hot dry rock geothermal energy. It creates an artificial geothermal reservoir by hydraulic fracturing which allows heat transmission through the fractures by circulating fluids as they extract heat from Hot Dry Rock (HDR) [4–6]. Fluid flow in fractured rock is a pivotal factor in determining the efficiency of heat extraction from geothermal energy. In EGS, the behavior of fluid flow and heat transfer within a fracture exerts a substantial influence on the effective extraction and recovery of energy [7–10]. Therefore, a comprehensive understanding of the heat transfer characteristics of fluid flow through fractured rocks is crucial for the design and stability assessment of EGS systems [11–15].

Researchers have mainly used two methods to study the process of seepage heat transfer in fractures: experiments at the core scale and numerical simulations at different scales. Bai et al. [16] investigated the heat transfer characteristics of fluids under different temperatures and flow rates and evaluated four current methods for calculating convective heat transfer coefficients. Through theoretical and numerical analysis of heat transfer in a conceptually simple three-dimensional fracture model with straightforward geometry, Klepikova et al. [17] found that flow channels can locally enhance thermal diffusivity. Their study demonstrates that cylindrical conduits achieve higher heat exchange efficiency between the fracture and the matrix compared to plane fractures of equivalent surface area, thereby improving overall heat transfer performance. Through the innovative application of three-dimensional printing technology, Huang et al. [18] successfully reconstructed fracture surfaces and quantitatively established the dominant influence of morphological characteristics and roughness parameters on heat transfer efficiency. Luo et al. [19] examined the permeability evolution of single-fracture granite under varying confining pressures and thermal conditions. Their findings revealed that increasing rock temperature led to a reduction in fracture hydraulic aperture, whereas the concomitant rise in fluid temperature enhanced hydraulic conductivity.

Due to the complexity of the principles underlying fluid flow and heat transfer experiments in fractured rock, as well as the technical difficulties in controlling boundary conditions and monitoring fractures, it is difficult to accurately characterize fluid flow and heat transfer processes in individual fractures [20]. Numerical simulations have proven instrumental in characterizing coupled fluid flow and heat transfer phenomena within stochastically distributed rock fractures, providing critical insights into the fundamental thermo-hydro-mechanical processes governing fractured rock systems. Their results demonstrate that rough fractures, compared to smooth fractures with identical mechanical apertures, may either enhance or diminish heat transfer. Notably, in fractures with variable apertures, increased flow velocities reduce fluid transit time through the channel, typically resulting in lower heat exchange efficiency than in smooth fractures of equivalent hydraulic aperture. Fox et al. [21] used 3D numerical modeling to demonstrate that variations in fracture apertures significantly influence geothermal heat production. Their results revealed that rough-walled fractures exhibit less efficient fluid-matrix heat exchange compared to planar surfaces due to reduced contact area. They concluded that aperture variability deteriorates the thermal performance of geothermal reservoirs. He et al. [22] simulated flow and heat transfer in a single fracture with varying roughness and compared the results with experimental data. Their findings revealed that rough surfaces improved heat transfer intensity, although this enhancement decreased as flow increased. Tan et al. [23] investigated the effect of heat transfer between the fluid and the fracture wall on the flow behavior in a single fracture. The process of heat flow through a fracture model created from a real rock surface was simulated by solving the Navier-Stokes equations and the energy conservation equation.

During the development of enhanced geothermal systems (EGS), the injection of cold fluid induces coupled thermo-hydro-mechanical-chemical (THMC) processes as it permeates the rock matrix and fracture networks. This process significantly alters the *in-situ* pore pressure, temperature distribution, and stress field, thereby affecting the mechanical behavior and long-term stability of the reservoir. Beyond rock deformation caused by thermal stress and pore pressure variations, mineral dissolution and precipitation play a critical role in governing heat extraction efficiency by dynamically altering fluid pathways. The importance of these coupled mechanisms has been well established in previous coupled THMC modeling studies. Building upon this foundation, Song et al. [24] employed THMC simulations to delineate the distinct contributions of mechanical and chemical processes to reservoir evolution, while Gao et al. [25] systematically evaluated and ranked the relative importance of different physical mechanisms governing thermal performance.

Recent advances in machine learning have demonstrated significant potential for rock characterization. These methods employ diverse approaches for predicting mechanical properties and identifying mineral composition. Tree-based ensemble methods have proven highly effective in estimating crucial geomechanical parameters such as uniaxial compressive strength directly from mineralogical data [26]. At the same time, deep learning techniques utilizing feature fusion of multi-modal microscopic images have achieved remarkable accuracy in automated lithology identification [27]. These methods provide not only high predictive accuracy but also valuable physical insights through feature importance analysis, offering efficient and objective alternatives to traditional laboratory techniques.

Numerical simulations of fracture seepage and heat transfer employ various 2D and 3D representations, each with distinct advantages and limitations. To address the rough structure of individual fractures, a mid-plane fracture model constructed from averaged fracture wall surfaces has been proposed as a replacement for plane fracture representations. This approach partially captures the roughness characteristics inherent in three-dimensional fractures [28]. While 3D modeling better captures void space irregularities and fracture wall roughness, it faces persistent challenges in mesh generation and computational efficiency, with typical model dimensions (10–250 mm) remaining significantly smaller than actual engineering scales. Although 2D models offer improved computational efficiency and are widely adopted in research and design, they often oversimplify the complexity of 3D fracture systems, and their accuracy requires systematic evaluation. In this context, this study positions the proposed simplified mid-plane fracture model as a pragmatic compromise within the HDR simulation methodology spectrum. Unlike equivalent continuum models that lose discrete flow path information or classical discrete fracture network approaches that neglect wall roughness, our model maintains a high-fidelity statistical representation of fracture topography. While full 3D simulations provide the highest geometric accuracy, their prohibitive computational cost limits parametric analysis. Our mid-plane approach bridges this gap, enabling efficient yet physically meaningful investigation of how fracture geometry and roughness control flow channeling and heat transfer efficiency, thereby providing crucial insights for upscaling processes in reservoir-scale models.

Building on this foundation, this study develops three types of fracture models: 3D fractures, 2D plane fractures and 2D rough mid-plane fractures. The differences between 2D plane fractures and 2D rough mid-plane fractures in their ability to simulate fluid flow in 3D fractures are evaluated. The temperature distribution and heat transfer coefficient (HTC) are analyzed under varying dimensional and roughness conditions. In addition, the influence of “X”-shaped and “V”-shaped intersecting fractures on fluid flow and heat transfer under various operational conditions is examined. The study aims to provide valuable insights for simplifying rock fracture geometries in numerical simulations, enhancing modeling accuracy in intersecting fracture network analysis, and understanding heat transfer in 3D intersecting rough fractures.

2 Materials & Methods

2.1 Basic Situation of Rock Specimens

The hot dry rock samples collected in the experiment were taken from the Gongtianzhen geothermal exploration area at the junction of the Mufu Mountain Range and the Miluo Sag Basin in the eastern Yueyang County, Hunan Province. The granite samples were analyzed by Bruker D8 X-ray diffractometer at different temperatures to determine the main mineral components and related physical parameters. Quantitative analysis at 25°C revealed the following composition (vol%): quartz (34%), mica (14%), albite (16%), anorthite (12%), and other minerals (13%), with observed grain sizes of 0.1–0.2 mm. The granite specimens exhibited a density of 2.7 g/cm^3 and uniaxial compressive strength of 132 MPa.

2.2 The Extraction of Rock Fracture Surface and the Generation and Reconstruction of Mid-Plane Fracture

2.2.1 Extraction of Fracture Surface Data

The surface morphology of the fracture was measured using the NANOVEA ST400 topography scanner which has an average sampling point distance of 0.04–0.1 mm and a measurement accuracy of 0.005–0.01 mm. The elevation data of both fracture surfaces were obtained by scanning, with an accuracy of 0.2 mm. The collected rock sample data were then processed for model construction. The data collection procedure included the following steps: The 3D surface morphology scanner was first positioned to ensure complete coverage of the rock fracture surface, followed by activation via the control software. The scanner acquires the fracture surface topography by emitting and capturing reflected optical signals, as illustrated in Fig. 1. The integrated sensor measures the time-of-flight or phase shift of reflected light to calculate point-wise distances. These distance measurements are subsequently converted into three-dimensional coordinates, generating a point cloud dataset. To mitigate boundary effects caused by the tensile test, extraneous noise and data from the specimen edges were removed. Only a central area with a fracture size of 40 mm × 40 mm is left. The resulting point cloud data accurately characterize the rock fracture surface morphology, enabling the subsequent construction of numerical models and analysis.

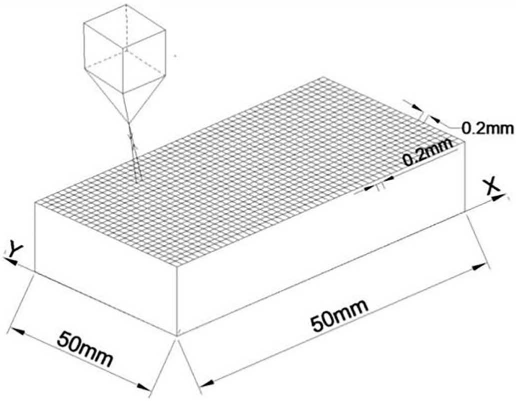

Figure 1: Schematic diagram of white beam scanning process

2.2.2 Generation and Reconstruction of Fractures

This study examines three fracture models: (1) a 3D fracture created by vertically displacing the top surface relative to the bottom surface, (2) a 2D plane fracture with spatially distributed aperture data assigned numerically, and (3) a 2D rough mid-plane fracture (Fig. 2) that more effectively characterizes the undulating median surface formed by connecting void centroids, compared to the plane counterpart.

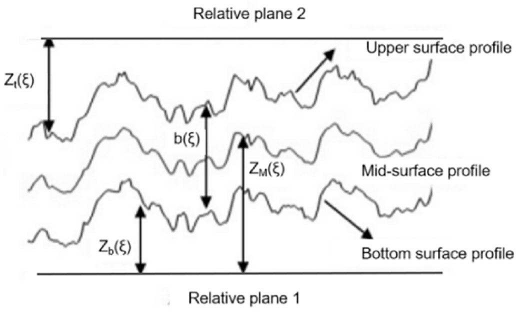

Figure 2: The top and bottom surfaces of the 3D fracture and the rough mid-plane

The theoretical foundation and justification for the simplified mid-plane model are firmly supported by a convergence of well-established concepts from surface physics, experimental rock mechanics, and structural theory. The core premise of representing the complex fracture geometry by a statistically averaged surface is directly underpinned by the work of Persson et al. [29], which establishes that the macroscopic behavior in contact and flow is governed by the statistical properties of surface roughness, not its microscopic details. This validates the representativeness of our averaged mid-plane. Furthermore, the physical relevance of this averaging operation is confirmed by the experimental findings of Boffa et al. [30], who demonstrated that fracture walls are typically highly correlated and mated, thereby ensuring that an averaged mid-plane is a meaningful geometric entity and not an artificial construct. Finally, the very principle of dimensional reduction via a mid-surface is a powerful and universally accepted methodology in computational mechanics, forming the cornerstone of the classical plate and shell theory [31]. By adopting this same conceptual framework, our approach leverages a proven strategy for efficiently simplifying complex 3D geometries into 2D representations without sacrificing the essential physics, thereby bridging a recognized gap between highly detailed but computationally prohibitive 3D models and oversimplified 2D approximations.

The vertical coordinates of the fracture's upper and lower walls at position ξ are denoted as $Z_t\,(\xi)$ and $Z_b(\xi)$, respectively. The rough mid-plane is mathematically defined as $Z_M(\xi) = (Z_t(\xi) + Z_b(\xi))/2$, representing the arithmetic mean of both fracture walls. The fracture aperture b(ξ) at the position ξ is defined as b(ξ) $= Z_t\,(\xi) - Z_b\,(\xi)$. The fracture aperture (local gap between fracture walls) varies spatially due to surface roughness of the fractured walls. Nine pairs of upper and lower fracture surfaces (F1–F9) were reconstructed from surface topography data of nine rock specimens. These surface pairs were subsequently utilized to generate corresponding 3D fracture models and mid-plane models, designated as Mid-1 through Mid-9. Plane aperture distributions were derived from nine sets of measured aperture data.

To systematically investigate the impact of varying surface roughness on fracture flow and heat transfer properties, this study expands the initial set of 9 mid-plane fractures to include 27 additional rough mid-plane fractures with different roughness levels. This is accomplished by vertically displacing the intermediate surface relative to its mean elevation, thereby increasing the height of surface protrusions while deepening contour depressions. Accordingly, the elevation $Z_N(\xi)$ of the rough mid-plane with progressively increasing roughness can be expressed as:

$$Z_N(\xi) = \{Z_M(\xi) - Z_M(\xi) \times M + Z_M(\xi) \tag{1}$$

where M represents the surface roughness amplification factor ($M = 1.5$, 2.0, and 2.5), and $Z_M(\xi)$ is the average elevation of the rough mid-plane (i.e., the initial elevation of the fracture's mid-plane). The methodology of scaling roughness amplitude to investigate its parametric influence is an established approach in numerical rock mechanics, as demonstrated by Xiong et al. [32], who magnified surface roughness to study its effect on hydraulic characteristics during shear. Fig. 3 demonstrates the reconstructed rough mid-plane of fracture F1, which possesses increased roughness amplitude while maintaining a consistent spatial morphology.

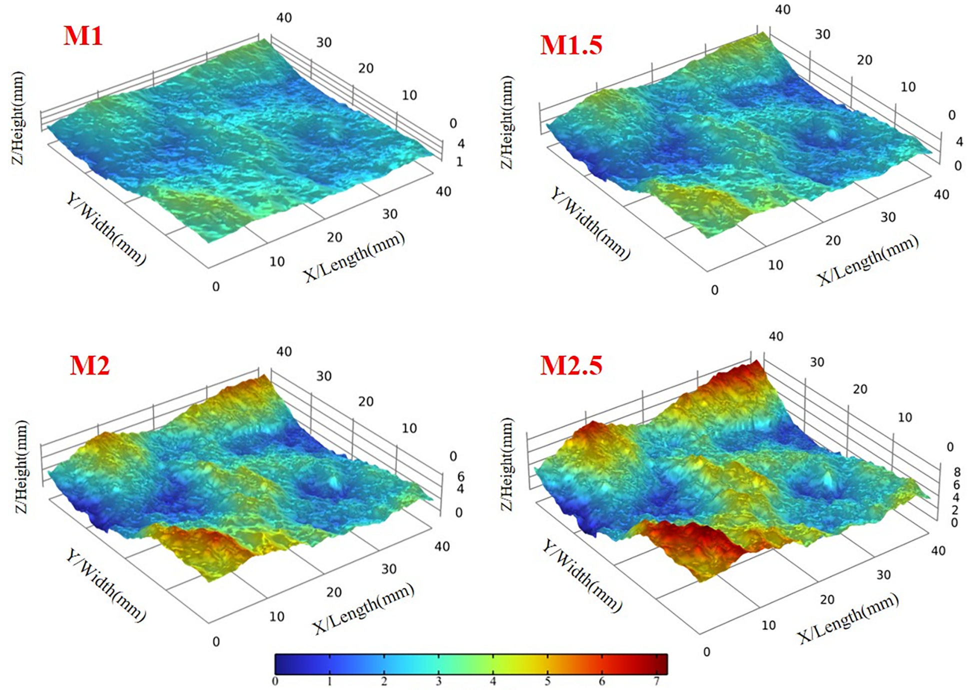

Figure 3: Mid-plane fractures of varying roughness

3 Results and Analysis

3.1 Characteristics of the Evolution of Permeability Differences between Different Types of Fractures

3.1.1 Seepage Field Equation

The flow behavior of steady, incompressible fluids within rock fractures is governed by the Navier-Stokes equations. To maintain physical consistency, these momentum equations must be coupled with and solved simultaneously with the continuity equation, expressed as follows:

$$\rho_f (\nabla u) \cdot u + \nabla P - \mu \nabla^2 u \tag{2}$$

$$\nabla \cdot u = 0 \tag{3}$$

where ρ_f is the fluid density, u is the velocity, μ is the dynamic viscosity, and p is the pressure.

The Reynolds equation is utilized to obtain solutions for 2D plane fracture and mid-plane fracture problems [24].

$$\nabla \cdot \left[\frac{\rho g b^3(x,y)}{12\mu} \right] = 0 \tag{4}$$

where $b(x,y)$ is the fracture aperture, which reflects the change of fracture in different spatial positions. For consistent model comparison, identical fracture apertures were employed in all simulations, including plane fractures, 2D midplane fractures, and 3D fractures. The model parameters are defined as follows: ρ_f is the fluid density, μ is the dynamic viscosity, and g is the gravitational acceleration.

Although the cubic law (Eq. (5)) is widely used to characterize fracture permeability, its applicability to 3D rough fractures is limited by significant errors, as the formulation originates from idealized planar fracture models. Given this limitation, recent advances have focused on refining the cubic law by incorporating fracture surface roughness to improve its predictive accuracy [33]. This approach enables reliable simulation of hydraulic conductivity in fractured rock masses, where the fracture transmissivity (T) is mathematically defined as the product of fracture conductivity and aperture width. The permeability T can also be inversely derived from Darcy's law, as expressed in Eq. (6) [34], where W is the fracture width, L represents the length of the flow path, and ΔH corresponds to the hydraulic head difference (or fluid pressure difference).

$$Q = -\left(\frac{Wb^3}{12\mu} \right) \frac{\Delta H}{L} \tag{5}$$

$$T = \frac{Q\mu L}{W\Delta H} \tag{6}$$

3.1.2 Differences in Hydraulic Characteristics of Different Forms of Fractures

The effect of fracture surface roughness (including internal and external undulations) is considered by comparing the permeability differences between 2D fractures (rough mid-plane fracture vs. plane fracture) and 3D fractures [35,36]. The relative permeability deviation (RD) was employed for quantitative assessment, calculated as follows:

$$RD_{pm} = \frac{T_P - T_m}{T_m} \times 100\% \tag{7}$$

$$RD_{mr} = \frac{T_m - T_r}{T_r} \times 100\% \tag{8}$$

$$RD_{pr} = \frac{T_p - T_r}{T_r} \times 100\% \tag{9}$$

$$T_{p/m/r} = b_h^3 / b_m^3 \tag{10}$$

where T_p, T_m and T_r represent the normalized permeability of plane fractures, initial mid-plane fractures, and 3D fractures, respectively. b_m^3 is the cube of the vertical aperture of the fracture, and $b_h^3 = 12Q\mu L/(W\Delta H)$ is the cube of the hydraulic aperture obtained from the flow simulation results.

Fig. 4 compares the differences in normalized permeability between simple plane fractures, rough mid-plane fractures (varying from M1 to M2.5), and complex 3D fractures. While all fracture types exhibit similar trends in permeability, their absolute values differ significantly. Notably, plane fractures demonstrate the highest permeability among all fracture types. Specifically, the plane fracture model from the F7 set reaches the maximum normalized permeability of 1.12. Mid-plane fractures with different roughness levels exhibit comparable permeability values, following a relatively consistent trend. However, their permeability gradually decreases from Tm-1.5 to Tm-2.5, indicating an inverse correlation between permeability and surface roughness. Overall, mid-plane fractures exhibit intermediate permeability—lower than plane fractures but higher than 3D fractures. In contrast, 3D fractures display the lowest and most variable normalized permeability, highlighting the substantial influence of geometric complexity on fluid flow behavior.

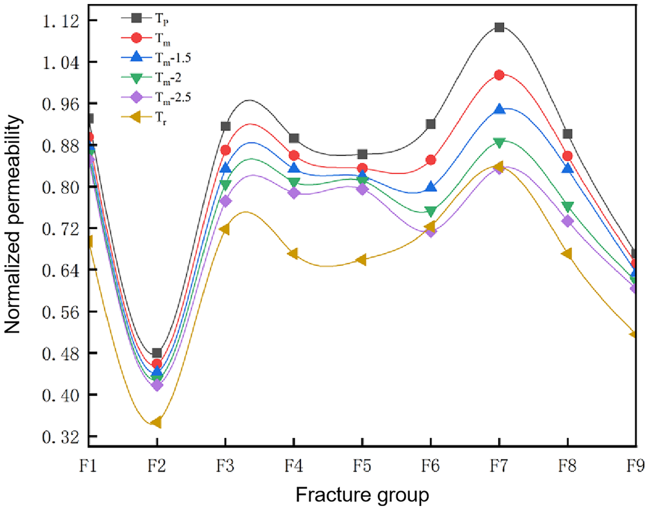

Figure 4: Normalized permeability: 2D (plane/mid-plane) vs. 3D fractures

As shown in Fig. 5, Statistical analysis of deviation distributions reveals that the RDmr values exhibit significantly greater dispersion compared to RDpr. Specifically, RDmr demonstrates a range of 17.80% to 32.24% (spanning 14.44 percentage points), whereas RDpr shows a narrower distribution between 27.30% and 38.26% (10.96 percentage points range). Furthermore, the RDpr distribution displays higher central tendency, with more than 50% of results clustered within the 30%–35% interval. In contrast, RDmr values are predominantly distributed across the 20%–30% range. Permeability deviation analysis of 3D fracture models indicates distinct differences between plane and rough mid-plane fractures. The mean permeability deviation (RDpr) for plane fractures is 32%, compared to approximately 25% for mid-plane fractures (RDmr), representing a 7% absolute difference.

Due to complex aperture geometry, three-dimensional (3D) fractures are commonly simplified as two-dimensional (2D) planar fractures with constant aperture in conventional Discrete Fracture Network (DFN) analyses. However, compared to simplified 2D representations, the actual complex aperture geometry of 3D fractures (e.g., surface roughness) induces greater flow resistance and creates more intricate flow pathways [37,38]. Consequently, traditional DFN approaches tend to overestimate the overall permeability and provide inadequate characterization of actual flow fields [39,40].

The results demonstrate that the permeability estimates derived from the mid-plane structural approximation align more closely with the reference 3D values than those from plane fracture models. This difference becomes particularly evident when directly comparing the two approximation approaches. The superior performance of the mid-plane model is attributed to its ability to preserve the essential geometric characteristics of fracture roughness, which fundamentally control flow channeling and hydraulic resistance. In contrast, the plane model, while computationally efficient, oversimplifies the fracture geometry, leading to less accurate predictions of flow behavior. This finding suggests that when modeling fracture flow systems, mid-plane structural approximations yield permeability estimates with smaller deviations from true values than plane fracture representations. The observed discrepancy is particularly pronounced when comparing these two structural approximations.

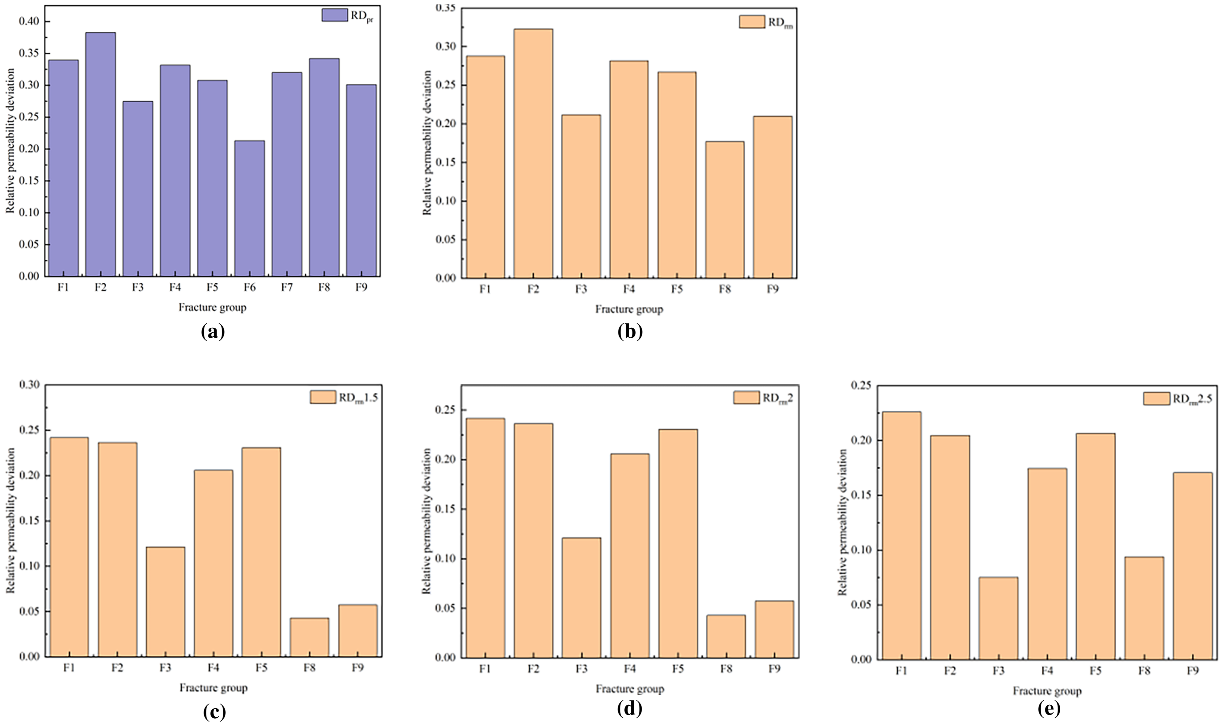

(a) (b)

(c) (d) (e)

Figure 5: Deviation in relative permeability between 3D fractures and other fracture types (a–e)

The roughness characteristics of the fracture aperture are determined from vertical aperture data, defined as the height difference between the upper and lower fracture surfaces. The corresponding statistical parameters are summarized in Table 1.

Analysis of the fracture aperture roughness characteristics reveals a strong linear correlation between the root mean square (RMS) and mean values (b_m) with fracture conductivity, yielding coefficient of determination (R^2) values of 0.76 and 0.84, respectively. As illustrated in Fig. 6, the statistical parameters of the aperture field (including RMS and b_m) exhibit a significant positive correlation with conductivity, indicating that fracture conductivity increases markedly with higher roughness parameters.

Surface roughness fundamentally alters the velocity field by introducing two critical effects: flow channeling and increased flow tortuosity. The geometric constrictions and expansions created by rough surfaces force the fluid to navigate through preferential pathways, resulting in a highly heterogeneous velocity distribution where high-velocity channels develop in wider aperture regions while stagnant or recirculation zones form behind roughness elements. Furthermore, the fluid must follow a longer, more tortuous path through a rough fracture compared to a smooth plane, which not only increases the effective flow distance but also enhances local mixing and fluid-solid interaction-phenomena that are entirely absent in planar fracture approximations.

Table 1: Characteristic parameters of aperture change

Aperture	RMS-ap (mm)	Bm (mm)
Ap 1	0.074	0.589
Ap 2	0.133	0.701
Ap 3	0.090	0.655
Ap 4	0.061	0.529
Ap 5	0.068	0.564
Ap 6	0.159	0.882
Ap 7	0.231	1.039
Ap 8	0.135	0.802
Ap 9	0.243	1.033

Note: The '-ap' suffix indicates aperture parameters (vertical height difference between fracture surfaces); bm: mean aperture.

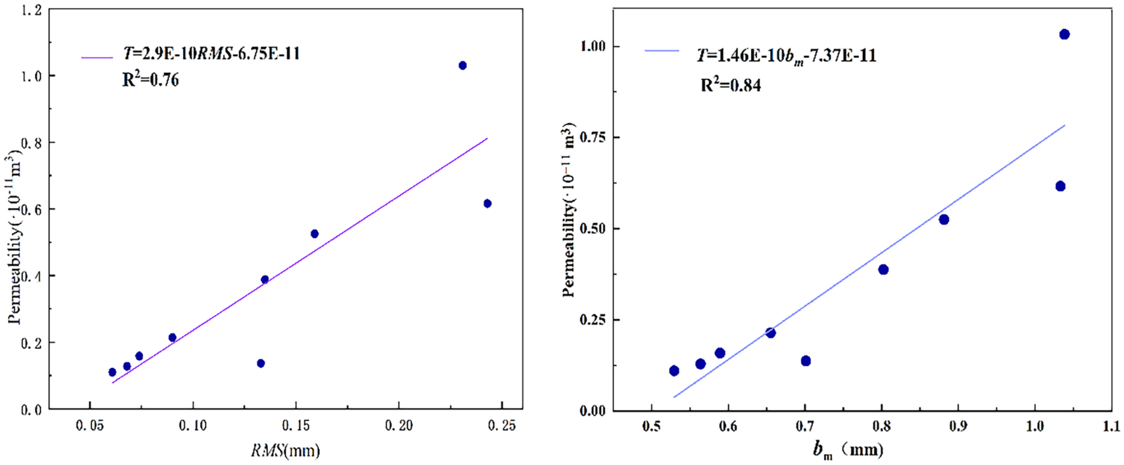

(a) (b)

Figure 6: Impact of aperture characteristics on permeability, (a) root mean square, (b) mean values

3.2 Characteristics of the Evolution of Heat Transfer Differences between Different Types of Fracture

3.2.1 Construction of Single Fracture Hydrothermal Coupling Numerical Model

The numerical model comprises a 40 mm × 40 mm × 30 mm domain containing a single fracture, which divides the rock mass into two symmetrical matrices. The fluid flow follows a unidirectional path along the y-axis, entering through the upstream fracture inlet ($y = 0$ mm) and exiting at the downstream outlet ($y = 40$ mm). The model consists of three distinct domains: the upper and lower domains represent the granite rock matrix, while the central domain constitutes the fluid-filled fracture, as shown in Fig. 7. Following the model geometry definition, the fracture flow is simulated as an incompressible laminar regime. A velocity inlet boundary condition with specified flow rate is applied at the fracture inlet (y = 0 mm), while the external rock surfaces are maintained at a constant temperature. Complete boundary condition specifications are provided in Table 2.

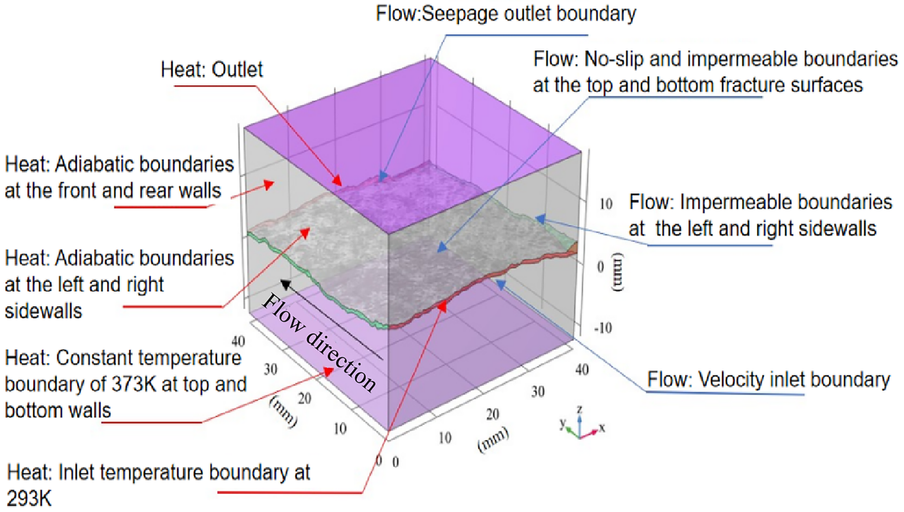

Figure 7: Initial and boundary conditions for heat transfer in fractured seepage flow

Table 2: Boundary condition parameters of fracture heat transfer model

Model boundary position	Fluid boundary condition	Temperature boundary condition
Fracture inlet	Velocity inlet: 0.05 m/s	Inlet temperature: 293 K
Fracture outlet	Velocity outlet: 1 MPa	Adiabatic boundary
Upper and lower walls	Non-slip, impermeable	Interfacial heat transfer
Fracture face	Non-slip, impermeable	Thermal insulation
Boundary face	Non-slip, impermeable	Thermal insulation
Inlet wall	Non-slip, impermeable	Thermal insulation
Outlet wall	Non-slip, impermeable	Thermal insulation
Top and bottom surface	Non-slip, impermeable	Constant wall temperature: 373 K

In numerical simulations, the mesh size and element count of a model are critical factors determining computational speed and accuracy. Identifying the appropriate area for dense mesh regions is crucial. If these regions are too small, they can only roughly represent the overall temperature distribution and fail to capture subtle temperature variations at the micro-scale. Conversely, excessively large dense mesh regions may lead to prolonged computational convergence, thereby compromising efficiency. Therefore, the optimal size for the dense mesh regions based on the specific geometry of the model and computational requirements is well selected.

Given that fractures are typically narrow (with apertures below 1 mm), different meshing strategies are required. Since heat exchange primarily occurs within the fractures, a denser mesh consisting of four layers of triangular elements was employed to enhance computational accuracy as illustrated in Fig. 8. This meshing strategy ensured high mesh quality (with an average element quality score above 0.6 and a minimum element quality above 0.2). To guarantee the accuracy of the numerical results, the fracture heat transfer model utilized over 1.5 million elements. To accommodate the diverse morphologies of fractures, triangular meshes were applied to both the 2D mid-plane and plane models. As fracture roughness increased, the mesh became more complex, leading to a higher element count. Mid-plane fracture models with different roughness levels exhibit significant variations in the number of mesh elements. In areas with complex fracture undulations, we increased the local mesh density, while in regions transitioning toward the boundaries, the mesh size gradually increased and the density decreased, achieving a balance between accuracy and efficiency. Fine meshes were applied around small-aperture regions, and boundary layers were used to address the no-slip boundary conditions at the fracture surfaces. The size of mesh elements ranged from 0.06 to 1.5 mm to adapt to different fracture morphologies. During the development of enhanced geothermal systems (EGS), the injection of cold fluid induces coupled thermo-hydro-mechanical-chemical The transient simulations were solved using a fully coupled approach with the MUMPS direct solver. Temporal discretization was implemented using the Backward Differentiation Formula (BDF) method, while an automatic adaptive control scheme was employed for time stepping with an initial step of 0.1 s, minimum step of 1×10^{-4} s, and maximum step of 1 s.

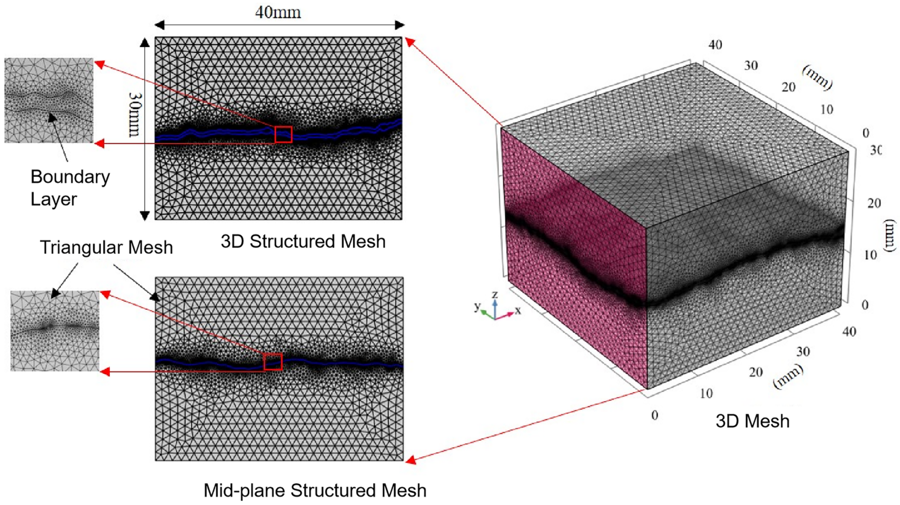

Figure 8: Numerical model meshes for different fracture types

For a simplified 2D fracture model, the equivalent heat transfer coefficient of a single rock fracture is determined using the formula proposed by Bai et al. [16]. The heat transfer coefficient of the rock specimen is calculated as follows:

$$h = \frac{C_{p,f}\rho q(T_{out} - T_{in})}{DL(T_c - \frac{(T_{out}+T_{in})}{2})} \tag{11}$$

where $C_{p,f}$ is the specific heat capacity of the fluid at constant pressure; ρ is the fluid density. T_c is the constant temperature of the outer wall of the fracture model; T_{in} and T_{out} are the inlet and outlet fluid temperatures, respectively. L is the path length of fluid flow. D is the length from the outer wall to the fracture.

3.2.2 The Difference in Heat Transfer Coefficient of Different Fractures

Fig. 9 shows the distribution of heat transfer coefficients (*h*) for different fracture types. The results demonstrate that the 3D fracture exhibits a higher heat transfer coefficient than the plane fracture and mid-plane fracture configurations. Among the mid-plane fractures, the mid-plane fracture with hm-2.5 shows the highest heat transfer coefficient, while hm-1 maintains consistently lower values. Notably, the heat transfer coefficient of mid-plane fractures increases with roughness, highlighting the significant influence of roughness on fracture heat transfer performance. In contrast, plane fractures display relatively uniform heat transfer coefficients across all fracture groups, with consistently lower values overall. These comparative results clearly illustrate the profound effect of both fracture geometry and surface roughness on heat transfer capacity.

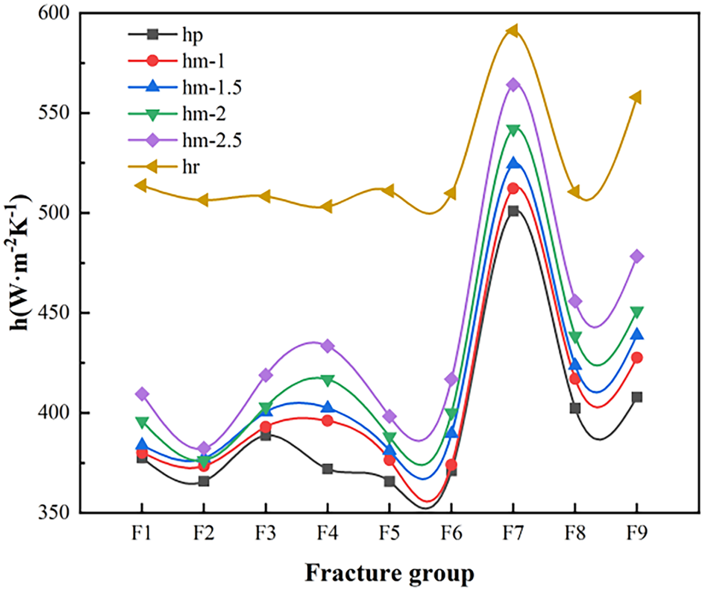

Figure 9: Heat transfer coefficient of three types of fractures

The observed trends in heat transfer coefficients provide compelling evidence that the rough mid-plane fracture models offer a substantially more accurate representation of 3D fracture behavior than plane approximations. While the plane fracture model fails to capture the essential thermo-hydrodynamic coupling mechanisms present in natural fractures, the mid-plane configuration successfully replicates the fundamental relationship between surface roughness and heat transfer enhancement characteristic of 3D systems. The progressive increase in heat transfer coefficient with roughness amplitude (hm-1 to hm-2.5) demonstrates that the mid-plane model effectively preserves the geometric complexity responsible for flow channeling and localized heat exchange intensification-phenomena that are inherently three-dimensional in nature. Furthermore, the convergence of heat transfer performance between the hm-2.5 mid-plane model and the reference 3D fracture indicates that the simplified representation maintains the critical surface area and tortuosity effects governing convective heat transfer, while achieving computational efficiency unattainable with full 3D simulations. This faithful reproduction of both qualitative trends and quantitative performance metrics establishes the rough mid-plane approach as a physically grounded alternative to conventional plane approximations, providing unprecedented capability for efficient yet accurate prediction of fracture-dominated thermal processes in HDR systems.

The parameters RMS and bm from the aperture statistical parameter table were fitted with the heat transfer coefficient of plane fractures to investigate the influence of aperture on heat transfer in fracture geometries. The thermal conductivity (h) exhibits a significant nonlinear dependence on the root-mean-square roughness (RMS) of fracture apertures as shown in Fig. 10a. The relationship is best characterized by a second-order polynomial function:

$$h = 383.259 - 431.29 \cdot RMS^1 + 3158.96 \cdot RMS^2, \mathrm{R}^2 = 0.77 \tag{12}$$

with a coefficient of determination (R^2) of 0.77, indicating that 77% of the variability in thermal conductivity can be explained by the aperture roughness. As illustrated in Fig. 10b, the effective thermal conductivity (h) and the mean fracture aperture (b_m) exhibit an exponential relationship, which is described by the function:

$$h = 362.69 + 0.209e^{-bm}/- 0.17, \mathrm{R}^2 = 0.72 \tag{13}$$

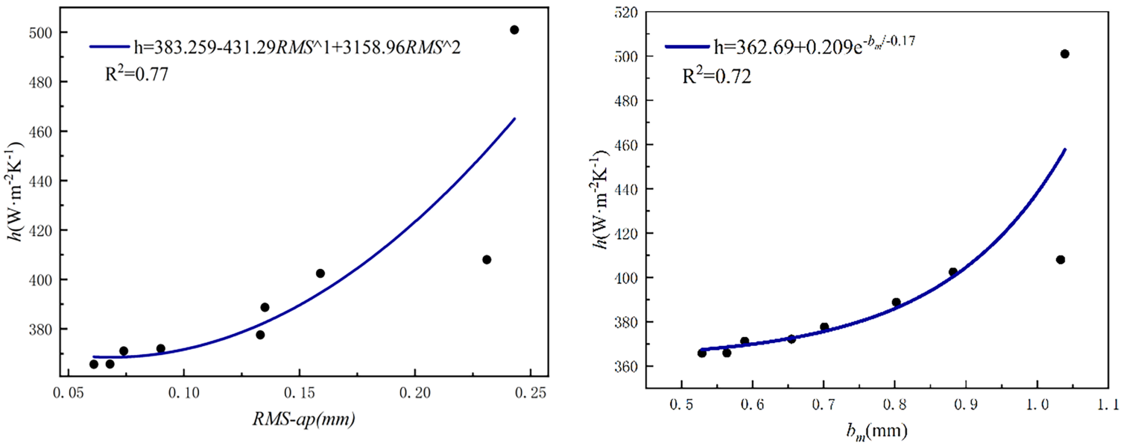

(a) (b)

Figure 10: Impact of aperture characteristics on thermal conductivity, (a) root-mean-square, (b) mean fracture aperture

3.2.3 The Effect of Roughness on Heat Transfer in Fractures

The roughness and structural heterogeneity of fracture surfaces, amplified by external bending forces, significantly extend fluid flow pathways. This prolonged fluid-rock interaction enhances heat transfer efficiency. Consequently, these fractures sustain higher temperatures during fluid circulation. This thermal behavior delays the onset of thermal breakthrough, a phenomenon characterized by heat depletion in the fracture-adjacent rock due to prolonged extraction. Without sufficient heat replenishment from the surrounding rock, the fluid temperature drops rapidly, leading to a sharp decline in production temperature. The enhanced surface roughness of fractures significantly elevates hydraulic resistance, exhibiting a proportional relationship with roughness amplitude. While higher flow rates facilitate greater heat extraction capacity, lower flow rates contribute to improved thermal stability at the production outlet, effectively delaying thermal breakthrough. Therefore, accurate numerical modeling of heat transfer in fractures must account for the coupling between flow velocity and surface roughness characteristics.

Steady-state simulations primarily reveal the equilibrium characteristics of the fracture system, enabling the quantification of effective hydraulic properties (e.g., permeability) and thermal resistance under stable flow conditions, while also identifying dominant flow paths and channeling patterns resulting from fracture geometry and roughness without the complicating effects of time-dependent thermal front propagation. Furthermore, this approach establishes a performance baseline for comparing different fracture models (planar, mid-plane, and 3D) under identical boundary conditions, thereby isolating purely geometric effects. In contrast, transient simulations capture the time-evolving dynamics critical for understanding the actual heat extraction process by tracking the temporal evolution of the thermal front, which reveals the progression of thermal drawdown and the phenomenon of thermal breakthrough. In essence, while steady-state results are invaluable for validating the geometric accuracy of our models and understanding the initial flow distribution, the transient simulations are indispensable for predicting the practical, time-dependent performance and longevity of an HDR system. The combination of both approaches in our study provides a comprehensive picture, from the intrinsic hydraulic properties to the dynamic heat extraction behavior.

As shown in Fig. 11, transient simulations of the fracture heat transfer model over 0–30 s were conducted to investigate the influence of different fracture morphologies on seepage and heat transfer. The outlet fluid temperature evolution exhibits three distinct phases: initial steady phase, decline phase, and subsequent steady phase. During the initial phase, the fluid temperature gradually increases through convective heat transfer until reaching thermal equilibrium with the surrounding rock. Subsequently, continuous heat extraction leads to the expansion of cooled regions, causing a sharp decrease in outlet temperature. Eventually, the rock mass temperature significantly decreases, resulting in reduced heat exchange efficiency and temperature stabilization. The simulation results indicate that at $t = 30$ s, the outlet temperatures for the 3D fracture, mid-plane fractures (M1–M2.5), and planar fracture are 306.10, 304.79–304.19, and 303.80 K, respectively. The thermal performance of mid-plane fractures falls between those of 3D and planar fractures, demonstrating their improved capability to represent actual heat transfer behavior. Fracture surface roughness directly governs heat exchange efficiency by altering flow field distribution and actual flow path length: rough surfaces enhance fluid perturbation and prolong fluid-rock contact time, thereby improving heat transfer performance, while smooth planar fractures exhibit inferior thermal performance due to streamlined flow paths.

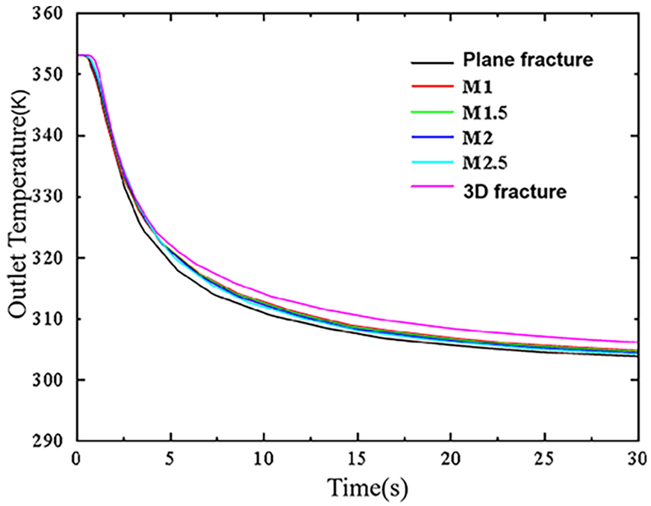

Figure 11: Temporal evolution of outlet fluid temperature for three fracture types

Fig. 12 compares the comparative temperature distributions at the representative cross-section (x = 20 mm) for three distinct fracture types. The thermal front progression demonstrates remarkable temporal consistency regardless of fracture morphology. In plane fractures with negligible surface roughness, the thermal front maintains a linear profile orthogonal to the flow direction and advances uniformly over time. In contrast, the rough surfaces of both mid-plane and 3D fractures result in heterogeneous thermal development and significant spatial variations in the heat conduction rates between the rock matrix and the fracture. For mid-plane fractures, elevated surface fluctuations ($M \geq 2.5$) intensify the surface bending, which reduces the distance to the matrix interface and enhances local thermal coupling. In contrast, plane fractures fail to replicate these phenomena observed in mid-plane configurations.

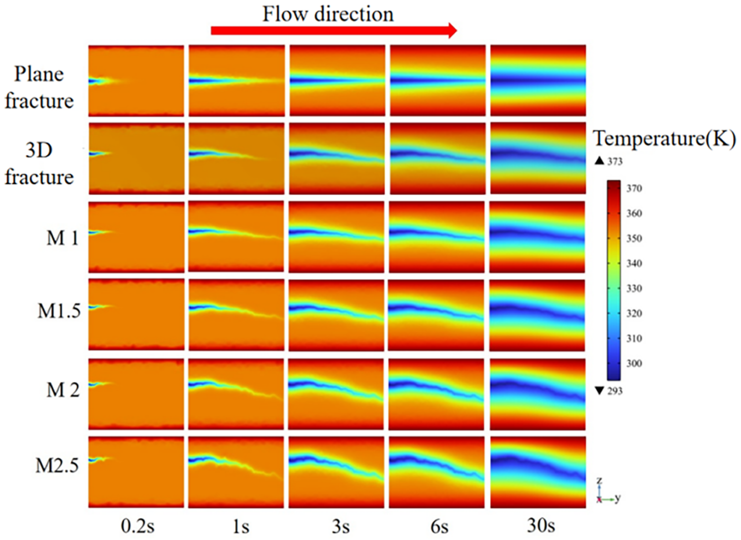

Figure 12: The temperature distribution of three types of fractures at the x = 20 mm section at different times

The impact of surface roughness on fracture surface temperature distribution was evaluated using steady-state and transient model analyses. The resulting temperature distribution patterns are presented in Fig. 13. Surface roughness induces irregularity in the infiltration front, leading to heterogeneous thermal distribution across the fracture plane. In mid-plane fractures, the surface morphology formed by bulges/depressions interacts with the flow behavior, inducing greater streamline curvature in the velocity field. The channeling effect induces flow focusing in mid-plane fractures with elevated surface roughness, leading to pronounced steepening of infiltration front edges. A comparison of the flow and temperature fields between the 3D and plane fracture models reveals that the mild channeling effect induced by aperture roughness in the plane model cannot adequately capture the pronounced flow heterogeneity and temperature variations observed in the 3D model with stronger surface undulations.

Based on these findings regarding temperature distribution and flow channeling, our results provide critical insights for practical HDR system design. The observed thermal heterogeneity and localized thermal front advancement in rough fractures suggest that conventional well spacing configurations may lead to significant portions of the reservoir being underutilized. To ensure adequate thermal sweep efficiency in naturally fractured reservoirs, closer well spacing should be considered to compensate for the flow channeling effects induced by surface roughness. Furthermore, the demonstrated trade-off between heat extraction capacity and thermal stability at different flow rates indicates that injection protocols should be optimized according to fracture roughness characteristics. For reservoirs with pronounced surface undulations, implementing moderate flow rates combined with cyclic injection schemes could help mitigate preferential flow paths while maintaining satisfactory heat extraction performance. Most importantly, the superior thermal performance observed in moderately rough fractures (M = 2.0–2.5) provides valuable guidance for stimulation strategy design. Rather than simply maximizing fracture complexity, stimulation techniques should aim to generate optimally rough fracture surfaces that balance the enhancement of heat exchange area with the maintenance of effective flow connectivity. These design implications, directly derived from our numerical observations, effectively bridge the gap between fundamental fracture behavior understanding and practical HDR engineering applications.

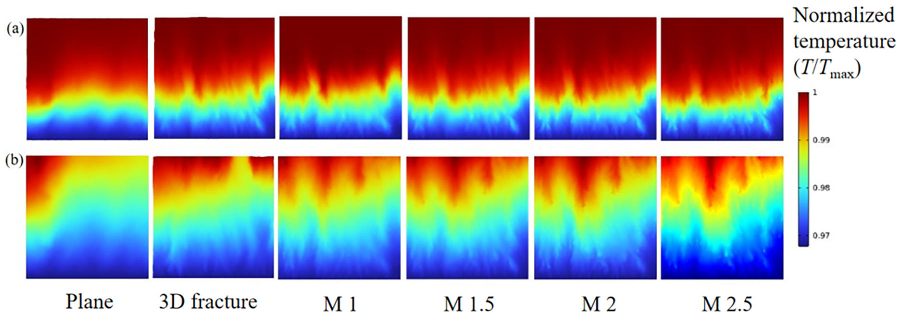

Figure 13: The infiltration front distribution of the same fracture in (a) transient (sixth second), (b) steady-state solution

3.3 Analysis of the Seepage Characteristics of Typical Intersecting Fractures

The interconnected fracture network significantly increases hydraulic path complexity while simultaneously reducing thermal exchange efficiency between adjacent rock matrices. Fluid flow is most preferential along the directions of fracture intersections, where the local morphology critically influences both the flow dynamics and heat transfer processes. Simply considering multiple fractures as overlapping fails to adequately capture their true influence on the overall mechanical behavior of the rock mass. While previous studies have examined seepage and heat transfer in single rough fractures, the influence of fracture intersections on these processes requires further exploration.

In this section, two representative fracture intersection geometries (“X”-type and “V”-type) were simulated to evaluate the effects of geometric structure on heat exchange efficiency. Additionally, the influences of fracture aperture and inlet flow velocity were also investigated. For computational efficiency, a 3D intersecting fracture model was generated based on mid-plane fracture representations. The model was specifically constructed using the M1 mid-plane fracture in F4, with both surfaces of the intersecting fractures formed by identical mid-plane fracture representations. The “X”-type fracture was created by rotating the mid-plane 15° counterclockwise and clockwise about the fracture centerline ($y = 20$ mm), forming a 30° intersection angle. The “V”-type fracture was formed by rotating the mid-plane 15° counterclockwise and clockwise about one edge ($y = 0$ mm), creating an asymmetric angular structure.

A comparative analysis was conducted to investigate the flow behavior characteristics between the two intersecting fracture configurations under varying velocity conditions. The upper fractures of both models were selected for detailed examination of flow distribution patterns. Fig. 14 presents the normalized velocity streamlines for both "X"- and "V"-type geometries at different apertures, with a constant injection velocity of 0.05 m/s.

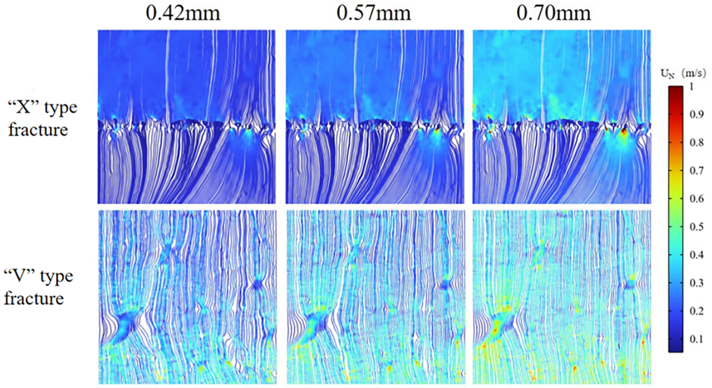

Figure 14: Streamline distribution in two types of rough fracture models at an injection rate of 0.05 m/s, where UN is the normalized velocity, UN = U/Um, Um is the average speed

Given the symmetrical configuration of both fracture types, the upper fractures in each model were selected to analyze and compare their flow behavior characteristics under varying velocity conditions. Fig. 14 illustrates the normalized velocity streamlines for the "X"- and "V"-type geometries at different apertures, with an injection velocity of 0.05 m/s. The flowfield is defined by $U = \sqrt{u_x^2 + u_y^2 + u_z^2}$, and its streamline diagram is shown as follows. Fig. 11 shows that the distribution of streamlines aligned with the flow direction exhibits considerable heterogeneity. With the increase of fracture aperture, the flow velocity of the fluid in a single fracture is enhanced, which is due to the non-uniform distribution of aperture in rough fracture, and a few channels become the dominant force of the flow. In the "X"-type model, the streamlines enter and exit circularly through some discrete local areas at the intersection, resulting in higher flow rates in these areas, thus forming a more distinct color area on the streamline diagram. In contrast, the "V"-type fracture exhibits a less pronounced channelization effect and reduced streamline curvature. However, beyond the intersection, the streamlines become significantly denser, indicating an enhanced influence of fracture intersections on fluid flow within the rock fractures. These findings demonstrate that fracture intersections markedly amplify the heterogeneity of internal flow dynamics in rock fractures.

3.4 Analysis of Heat Transfer Characteristics of Typical Intersecting Fractures

3.4.1 Temperature Distribution Characteristics of 3D Intersecting Fractures

In order to minimize extraneous factors, both intersecting fracture models were designed with identical fracture surface geometries. The geometric equivalence in fracture area eliminates potential result bias from matrix contact area variations. The simulation investigates the evolution of temperature distribution under four distinct injection velocities to enable systematic comparative analysis. For more accurate observation and comparison of the heat exchange process within the fracture, the y-z plane cross-section at x = 15 mm is selected. This ensures the observation surface lies within the 30° intersecting fracture zone, allowing clear analysis of the temperature field.

Fig. 15 shows the temperature distribution of the two types of fractures. During low-temperature water injection, a pronounced cooling zone initially develops near the fracture inlet. The low-temperature zone progressively expands with sustained water flow, demonstrating convective heat transfer from the rock matrix to the flowing water, a phenomenon consistently observed in both fracture models. Notably, in "X" model, the infiltration fronts exhibit asymmetric distribution patterns across the upper and lower surfaces of the fracture intersection area during both initial (t = 0 s) and intermediate (t = 6 s) stages. This observed heterogeneity in front propagation likely stems from inherent inconsistencies between the upper and lower contact surfaces within the intersecting fracture network, potentially attributable to the natural roughness and geometric variability of fracture surfaces. Moreover, the segmentation of the model grid may lead to a minor overlap between the upper and lower sections of the fracture model. This overlap consequently causes a discrepancy in the morphological distribution of the infiltration front between these two segments when observed at identical time intervals. As time goes on, the distribution of infiltration front in the two fracture models tends to be consistent. This indicates that in the long-term flow process, the heterogeneity characteristics that originally existed in the fracture are gradually diluted by the heat exchange of the water and tend to reach a dynamic thermal equilibrium state.

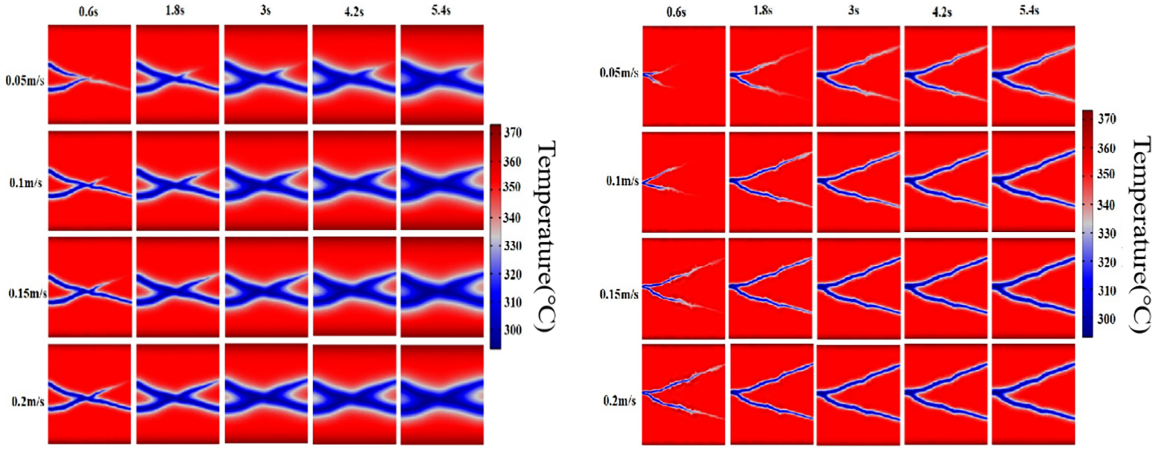

(a) (b)

Figure 15: The variation of temperature distribution with time in two types of intersecting fracture models (a, b)

A comparative analysis of temperature distributions is performed between 'X'-type and 'V'-type intersecting fractures as shown in Fig. 16, focusing on the Z-X intermediate section (fracture intersection zone) and its corresponding thermal field characteristics. The infiltration front morphology and heat transfer characteristics demonstrate remarkable consistency across all fracture surfaces in "V"-type fractures under varying injection rates. In contrast, "X"-type fractures exhibit significant variations in infiltration front geometry, with these differences becoming particularly pronounced at higher injection rates. At specific conditions (0.05 m/s injection rate and 0.57 mm aperture), the intersection region of "X"-type fractures displays distinctive thermal distribution patterns. The non-uniform aperture distribution generates complex channel flow, leading to highly heterogeneous infiltration front development. This flow pattern generates rotational streamlines within the intersection zone, producing an irregular elliptical cold front that propagates laterally along the fracture branches over time.

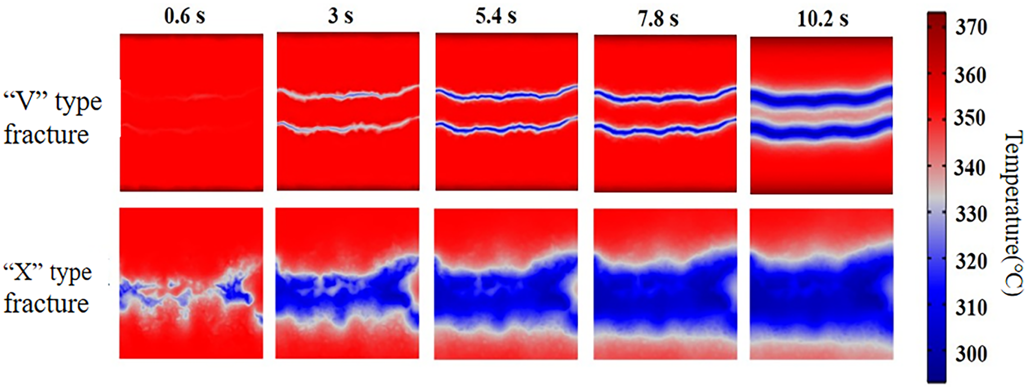

Figure 16: Variation of temperature distribution of two types of intersecting fracture in Z-X intermediate section with time

The four-branch geometry of X-type intersections creates a central confluence zone where flow paths from multiple directions converge and interact. This convergence enhances fluid mixing and disrupts the development of thick thermal boundary layers, effectively increasing the active heat transfer perimeter. In contrast, the simpler V-type configuration primarily facilitates linear flow convergence with limited lateral interaction. Meanwhile, the orthogonal nature of X-type intersections creates more uniform flow distribution across the fracture network, allowing thermal energy to be extracted from a larger rock volume. The increased path complexity also extends the effective fluid residence time within the critical intersection region, enabling more complete thermal equilibration. Furthermore The X-type configuration naturally forms a larger central contact area where multiple fractures interact simultaneously with the fluid. This geometric characteristic creates a more complex and extensive heat exchange interface compared to the relatively limited contact zone in V-type intersections.

3.4.2 The Influence of Injection Flow Rate

Fig. 17 illustrates the temporal evolution of effluent temperature at the fracture outlet for different injection velocities. The temperature decline exhibits three distinct phases: pre-stabilization, recession, and post-stabilization. Higher injection rates accelerate both the cooling rate and the transition to the recession phase, significantly reducing the time required to reach this stage. The observed phenomenon can be attributed to the fact that higher injection flow rates facilitate greater fluid flux through the fracture per unit time. This enhanced fluid flow promotes more efficient heat extraction, leading to accelerated cooling within the fracture and an earlier onset of the recession stage. Notably, the final stabilized temperatures exhibit an inverse dependence on injection rates, with lower flow rates yielding higher equilibrium temperatures. At lower injection velocities, enhanced thermal interaction between the fracture fluid and surrounding rock promotes more complete heat exchange, leading to a more uniform temperature distribution within the fracture and consequently a higher equilibrium temperature. In contrast, higher flow rates induce rapid heat extraction, preventing the fracture system from attaining thermal equilibrium with the rock matrix within a limited timeframe, thereby resulting in a lower stabilized temperature. These observations demonstrate that the outlet fluid temperature is strongly dependent on the injection rate, with increased flow rates accelerating thermal decline.

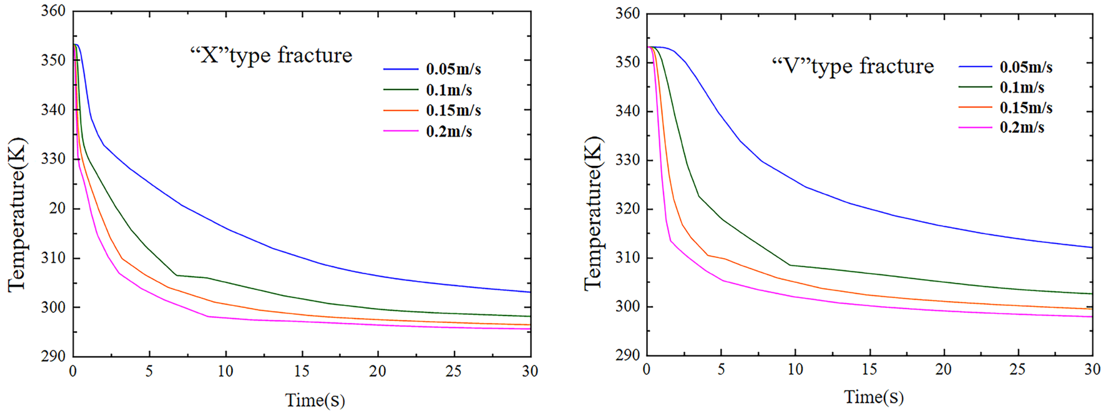

(a) (b)

Figure 17: Variation of outlet temperature of “X” type fracture (a) and “V” type fracture (b) with time under different injection rates

3.4.3 The Influence of Aperture Size

Fig. 18 illustrates the temporal evolution of fracture outlet temperature under different apertures at an injection velocity of 0.05 m/s. For both fracture types, the outlet temperature exhibits three distinct phases: pre-stabilization, recession, and post-stabilization. As the aperture increases, the duration of the recession phase shortens, accompanied by a more rapid temperature decline. This phenomenon occurs because increased fracture apertures simultaneously enlarge both the void volume and the fluid-rock contact area, thereby improving thermal transfer efficiency. Consequently, fractures with larger apertures experience accelerated cooling and an earlier onset of the recession phase. Furthermore, the results demonstrate an inverse correlation between aperture size and final stabilized temperature. Reduced fracture apertures diminish both the fluid storage capacity and interfacial contact area, consequently constraining conductive and convective heat transfer processes. Consequently, narrow-aperture fractures retain elevated equilibrium temperatures relative to wider fractures due to their constrained heat transfer capacity.

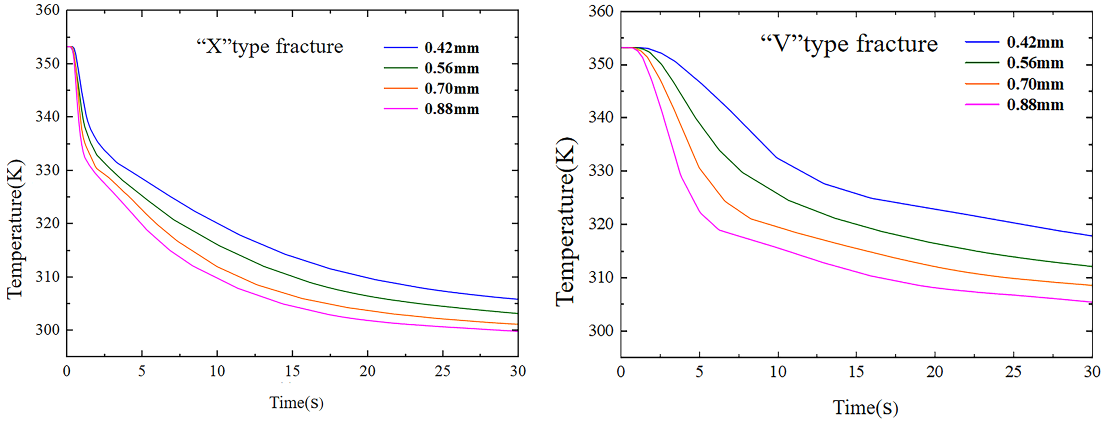

(a) (b)

Figure 18: Temporal variations in outlet temperature for (a) “X”-type and (b) “V”-type fractures with different apertures

Temporal evolution of outlet temperature for the two fracture types reveals significant differences. Both fracture types undergo three distinct stages, though the timing of these stages differs. Comparative analysis shows that the recession stage typically lasts longer in “X”-type fractures than in “V”-type fractures. This divergence stems from fracture morphology-dependent modulation of fluid flow patterns and associated thermal transport mechanisms. Specifically, the intersecting structure of “X”-type fractures provides additional flow and heat exchange paths, enhancing heat dispersion and prolonging the recession stage. The prolonged thermal recession results from cross-structure-induced modifications to heat transfer efficiency and dynamic equilibrium conditions, where the intersecting geometry creates competing thermal transport mechanisms. In contrast, the reduced geometric complexity of ‘V’-type fractures constrains heat transfer to predominantly linear flow paths, limiting thermal exchange efficiency. As a result, heat accumulates and dissipates more rapidly, shortening the recession stage duration.

4 Discussion

The comparative analysis presented in this study demonstrates that the proposed mid-plane fracture model achieves a superior balance between computational efficiency and physical accuracy. Permeability estimates derived from the mid-plane structural approximation show significantly better agreement with reference 3D values than those from planar fracture models. This enhanced performance is directly attributed to the model’s capacity to preserve the essential geometric characteristics of fracture roughness, which fundamentally govern flow channeling and hydraulic resistance. In contrast, the planar model, while computationally efficient, oversimplifies the fracture geometry, leading to less accurate predictions of flow behavior.

Consistent with the flow characteristics, the analysis of heat transfer coefficients provides compelling evidence that the rough mid-plane models offer a substantially more accurate representation of 3D thermo-hydrodynamic behavior. The plane fracture model fails to capture the essential coupling mechanisms present in natural fractures, whereas the mid-plane configuration successfully replicates the fundamental relationship between surface roughness and heat transfer enhancement. The observed progressive increase in heat transfer coefficient with roughness amplitude (from hm-1 to hm-2.5) demonstrates that the mid-plane model effectively preserves the geometric complexity responsible for flow channeling and localized heat exchange intensification-phenomena that are inherently three-dimensional in nature. The convergence of heat transfer performance between the hm-2.5 mid-plane model and the reference 3D fracture indicates that this simplified representation maintains the critical surface area and tortuosity effects governing convective heat transfer, while achieving computational efficiency unattainable with full 3D simulations.

The investigation of fracture intersections reveals that geometric configuration profoundly influences system-level thermal performance. The four-branch geometry of X-type intersections creates a central confluence zone where flow paths from multiple directions converge and interact. This multi-directional convergence enhances fluid mixing and disrupts the development of thick thermal boundary layers, effectively increasing the active heat transfer perimeter. Furthermore, the orthogonal nature of X-type intersections promotes more uniform flow distribution across the fracture network, allowing thermal energy to be extracted from a larger rock volume. The increased path complexity also extends the effective fluid residence time within the critical intersection region, enabling more complete thermal equilibration. Additionally, the X-type configuration naturally forms a larger central contact area where multiple fractures interact simultaneously with the fluid, creating a more complex and extensive heat exchange interface compared to the relatively limited contact zone in V-type intersections. These combined geometric advantages explain the observed 40%–60% greater effective heat conduction area of X-type configurations, highlighting their superior heat transfer characteristics.

These findings have significant implications for the design and numerical modeling of HDR systems. The validated mid-plane approach provides a reliable methodology for efficient parametric studies of fracture network properties, enabling more accurate prediction of reservoir-scale behavior without the prohibitive computational cost of full 3D simulations. The identified relationship between intersection geometry and thermal efficiency offers practical guidance for well placement strategies and reservoir stimulation design, suggesting that engineering practices should aim to create interconnected fracture networks with optimal intersection characteristics rather than simply maximizing fracture density. However, it is important to acknowledge that while the mid-plane model successfully captures first-order roughness effects, its application to field-scale reservoirs requires further development to address multi-physics coupling and upscaling challenges inherent in complex fracture networks.

The analysis of thermal transport in intersecting fractures reveals fundamentally different behaviors between short-term and long-term operational scenarios. In the short-term phase, thermal performance is predominantly controlled by advective heat transfer through preferential flow paths established by the intersection geometry. fractures with higher connectivity (e.g., The efficient extraction of geothermal energy from fractured hot dry rock, X-type intersections) exhibit rapid heat extraction but also accelerated thermal front propagation through these dominant channels. Conversely, in the long-term phase, the system behavior transitions to being governed by conductive heat recharge from the rock matrix and the evolution of thermally-induced flow paths. Our results indicate that while geometrically complex intersections may provide superior initial heat production, they often develop localized thermal depletion zones more quickly. Fracture intersections with more tortuous flow paths, though initially less efficient, demonstrate better sustainability in long-term simulations due to more uniform thermal drawdown and continued conductive replenishment from a larger rock volume. This temporal distinction carries critical implications for EGS design: short-term efficiency favors highly connected fracture networks, while long-term sustainability necessitates a balance between connection quality and distributed heat source utilization.

5 Conclusion

The rough intermediate surface of the fracture is represented by the average value of the upper and lower surfaces, expressed as $Z_M(\xi) = (Z_t(\xi) + Z_b(\xi))/2$. A comparative analysis of the permeability and heat transfer coefficient is conducted for three fracture models, with a focus on the effects of fracture surface roughness and aperture on seepage heat transfer. Furthermore, the influence of fracture geometry on seepage heat transfer is systematically investigated, particularly emphasizing the role of fracture opening and inlet injection velocity in determining heat exchange efficiency. The main conclusions of this work are as follows:

(1) The F7 group (plane fractures) demonstrates the highest normalized permeability (1.106), whereas the F2 group (3D fractures) exhibits the lowest value (0.347). Mid-plane fractures display intermediate permeability, decreasing with surface roughness. As for thermal performance, 3D fractures achieve the highest heat transfer coefficient (F7 group), surpassing plane fractures (F5 group) by 61.7%. Mid-plane fractures follow an intermediate trend, with heat transfer efficiency increasing with roughness.

(2) Plane fracture conductivity increases with average aperture (b_m), while the heat transfer coefficient (h) follows an exponential decay relationship with b_m. The mid-plane fracture

model better captures the non-uniform flow and temperature fields observed in 3D fractures, especially at larger surface fluctuation amplitudes. Compared to plane fractures, the mid-plane model provides more consistent results with 3D fractures while maintaining superior computational efficiency for realistic fracture simulations.

(3) Fracture aperture critically governs both seepage and temperature field distributions. Fracture intersections enhance connectivity and modify flow patterns. In “V”-type fractures, aperture enlargement leads to uneven streamline distributions and localized velocity increases. In contrast, “X”-type fractures amplify intersection velocities and increase downstream streamline density. Both aperture size and injection rate emerge as key controls on outlet temperature and heat decay duration, offering optimization potential for geothermal systems. Notably, intersection geometry significantly impacts transport pathways, with “X”-type configurations demonstrating superior thermal performance to “V”-type fractures.

Scaling numerical insights to actual hot dry rock reservoirs faces four primary challenges: (1) extending beyond thermo-hydrodynamic coupling to address full THMC interactions across fracture networks; (2) upscaling from single-fracture behavior to emergent network phenomena through advanced methodologies; (3) characterizing natural heterogeneity in aperture, roughness and connectivity beyond parametric approximations; and (4) addressing operational constraints including dynamic flow management and long-term sustainability assessment. While these challenges represent important research frontiers, our work establishes a validated fundamental-scale foundation for future field-scale model development.

Acknowledgement: Not applicable.

Funding Statement: This work was supported by the National Natural Science Foundation of China (Nos. 52174127, 52374137, 42502170), the Youth Innovation Team Project of Shaanxi University, and the Outstanding Youth Science Fund Project of Shaanxi (2023-JC-JQ-42).

Author Contributions: The authors confirm contribution to the paper as follows: Xinrui Gao: Writing—original draft; Li’an Tang: Writing—review & editing; Wenyu Lv: Project administration, Methodology; Chao Lyu: Writing—review & editing, Methodology, Investigation, Validation; Yongping Wu: Visualization, Formal analysis; Panshi Xie: Conceptualization, Methodology. All authors reviewed the results and approved the final version of the manuscript.

Availability of Data and Materials: Data available on request from the authors.

Ethics Approval: Not applicable.

Conflicts of Interest: The authors declare no conflicts of interest to report regarding the present study.

References

1. Kang FC, Tang CA, Li YC, Li TJ, Men JL. Challenges and opportunities of enhanced geothermal systems: a review. Chin J Eng. 2022;44(10):1767–77. (In Chinese). doi:10.13374/j.issn2095-9389.2022.04.07.004.
2. Vidana Pathiranagei S, Gratchev I, Kong R. Engineering properties of four different rocks after heat treatment. Geomech Geophys Geo Energy Geo Resour. 2021;7(1):16. doi:10.1007/s40948-020-00211-8.

3. Zeng C, Tang F, Yuan Y, Cao X, Haghighat F, Panchabikesan K. Thermal performance of energy diaphragm wall (EDW) adjacent to air-conditioned space from the underground-engineering perspective. Geothermics. 2021;91:102044. doi:10.1016/j.geothermics.2021.102044.
4. Xue Z, Ma H, Wei Y, Wu W, Sun Z, Chai M, et al. Integrated technological and economic feasibility comparisons of enhanced geothermal systems associated with carbon storage. Appl Energy. 2024;359(8):122757. doi:10.1016/j.apenergy.2024.122757.
5. Liu J, Zhao P, Peng J, Xian H. Insight into the investigation of heat extraction performance affected by natural fractures in enhanced geothermal system (EGS) with THM multiphysical field model. Renew Energy. 2024;231(9):121030. doi:10.1016/j.renene.2024.121030.
6. Li X, Zhang F, Xiu N, Weng D, Cai B, Fu H. Shear-induced permeability evolution of natural fractures in granite: implications for stimulation of EGS reservoirs. Eng Geol. 2024;338:107629. doi:10.1016/j.enggeo.2024.107629.
7. Zhou L, Zhu Z, Xie X, Hu Y. Coupled thermal-hydraulic–mechanical model for an enhanced geothermal system and numerical analysis of its heat mining performance. Renew Energy. 2022;181:1440–58. doi:10.1016/j.renene.2021.10.014.
8. Wang G, Ma X, Song X, Li G. Modeling flow and heat transfer of fractured reservoir: implications for a multi-fracture enhanced geothermal system. J Clean Prod. 2022;365(1):132708. doi:10.1016/j.jclepro.2022.132708.
9. Shah M, Prajapati M, Yadav K, Sircar A. A comprehensive review of geothermal energy storage: methods and applications. J Energy Storage. 2024;98(4):113019. doi:10.1016/j.est.2024.113019.
10. Zhang Q, Dahi Taleghani A. Real-time temperature monitoring and flow control for improved heat extraction in enhanced geothermal systems. Energy. 2025;314(1):134274. doi:10.1016/j.energy.2024.134274.
11. Asai P, Panja P, McLennan J, Deo M. Effect of different flow schemes on heat recovery from enhanced geothermal systems (EGS). Energy. 2019;175:667–76. doi:10.1016/j.energy.2019.03.124.
12. Ma Y, Gan Q, Zhang Y, Huang Y. Experimental research on the heat transfer characteristics of fluid flowing through rock with intersecting fractures. Geothermics. 2023;107(7):102587. doi:10.1016/j.geothermics.2022.102587.
13. Wang JY, Kong YL, Duan ZF, Zhang JX, Luo XL, Huang YH, et al. Geothermal energy exploitation and storage in coal field under the dual carbon goal. Coal Geol Explor. 2023;51(2):1–11. (In Chinese). doi:10.12363/issn.1001-1986.23.02.0104.
14. Anya B, Mohammadpourfard M, Akkurt GG, Mohammadi-Ivatloo B. Exploring geothermal energy based systems: review from basics to smart systems. Renew Sustain Energy Rev. 2025;210(12):115185. doi:10.1016/j.rser.2024.115185.
15. Li ZW, Feng XT, Zhang YJ, Zhang C, Xu TF, Wang YS. Experimental research on the convection heat transfer characteristics of distilled water in manmade smooth and rough rock fractures. Energy. 2017;133(32):206–18. doi:10.1016/j.energy.2017.05.127.
16. Bai B, He Y, Li X, Li J, Huang X, Zhu J. Experimental and analytical study of the overall heat transfer coefficient of water flowing through a single fracture in a granite core. Appl Therm Eng. 2017;116(10): 79–90. doi:10.1016/j.applthermaleng.2017.01.020.
17. Klepikova MV, Le Borgne T, Bour O, Dentz M, Hochreutener R, Lavenant N. Heat as a tracer for understanding transport processes in fractured media: theory and field assessment from multiscale thermal push-pull tracer tests. Water Resour Res. 2016;52(7):5442–57. doi:10.1002/2016WR018789.
18. Huang Y, Zhang Y, Yu Z, Ma Y, Zhang C. Experimental investigation of seepage and heat transfer in rough fractures for enhanced geothermal systems. Renew Energy. 2019;135:846–55. doi:10.1016/j.renene.2018.12.063.
19. Luo J, Zhu Y, Guo Q, Tan L, Zhuang Y, Liu M, et al. Experimental investigation of the hydraulic and heat-transfer properties of artificially fractured granite. Sci Rep. 2017;7(1):39882. doi:10.1038/srep39882.

20. Tavakkoli Osgouei Y, Akin S. Experimental and numerical study of flow and thermal transport in fractured rock. Heat Mass Transf. 2021;57(6):1053–68. doi:10.1007/s00231-020-03001-w.
21. Fox DB, Koch DL, Tester JW. The effect of spatial aperture variations on the thermal performance of discretely fractured geothermal reservoirs. Geotherm Energy. 2015;3(1):21. doi:10.1186/s40517-015-0039-z.
22. He R, Rong G, Tan J, Cheng L. Numerical investigation of fracture morphology effect on heat transfer characteristics of water flow through a single fracture. Geothermics. 2019;82(4):51–62. doi:10.1016/j.geothermics.2019.05.014.
23. Tan J, Rong G, He R, Yang J, Peng J. Numerical investigation of heat transfer effect on flow behavior in a single fracture. Arab J Geosci. 2020;13(17):851. doi:10.1007/s12517-020-05824-7.
24. Song G, Song X, Xu F, Li G, Shi Y, Ji J. Contributions of thermo-poroelastic and chemical effects to the production of enhanced geothermal system based on thermo-hydro-mechanical-chemical modeling. J Clean Prod. 2022;377(4):134471. doi:10.1016/j.jclepro.2022.134471.
25. Gao X, Qiao Y, Wang Z, Li T. Production potential assessment of enhanced geothermal system with thermos-hydraulic-mechanical-chemical mechanism in hot dry rock. Energy Convers Manag. 2024;309:118410. doi:10.1016/j.enconman.2024.118410.
26. Hussain J, Fu X, Chen J, Ali N, Iqbal SM, Hussain W, et al. Estimation of rock strength parameters from petrological contents using tree-based machine learning techniques. AI Civ Eng. 2025;4(1):4. doi:10.1007/s43503-024-00047-1.
27. Ma W, Han T, Xu Z, Lin P. Feature fusion of single and orthogonal polarized rock images for intelligent lithology identification. AI Civ Eng. 2025;4(1):5. doi:10.1007/s43503-025-00049-7.
28. Brush DJ, Thomson NR. Fluid flow in synthetic rough-walled fractures: Navier-Stokes, Stokes, and local cubic law simulations. Water Resour Res. 2003;39(4):2002WR001346. doi:10.1029/2002WR001346.
29. Persson BNJ, Albohr O, Tartaglino U, Volokitin AI, Tosatti E. On the nature of surface roughness with application to contact mechanics, sealing, rubber friction and adhesion. J Phys Condens Matter. 2005;17(1):R1–62. doi:10.1088/0953-8984/17/1/R01.
30. Boffa JM, Allain C, Hulin JP. Experimental analysis of fracture rugosity in granular and compact rocks. Eur Phys J AP. 1998;2(3):281–9. doi:10.1051/epjap:1998194.
31. Reddy JN. Theory and analysis of elastic plates and shells. Boca Raton, FL, USA: CRC Press; 2006.
32. Xiong X, Li B, Jiang Y, Koyama T, Zhang C. Experimental and numerical study of the geometrical and hydraulic characteristics of a single rock fracture during shear. Int J Rock Mech Min Sci. 2011;48(8): 1292–302. doi:10.1016/j.ijrmms.2011.09.009.
33. Lee SH, Lee KK, Yeo IW. Assessment of the validity of Stokes and Reynolds equations for fluid flow through a rough-walled fracture with flow imaging. Geophys Res Lett. 2014;41(13):4578–85. doi:10.1002/2014gl060481.
34. Nazridoust K, Ahmadi G, Smith DH. A new friction factor correlation for laminar, single-phase flows through rock fractures. J Hydrol. 2006;329(1–2):315–28. doi:10.1016/j.jhydrol.2006.02.032.
35. Zimmerman RW, Bodvarsson GS. Hydraulic conductivity of rock fractures. Transp Porous Medium. 1996;23(1):1–30. doi:10.1007/BF00145263.
36. Li Y, Huang R. Relationship between joint roughness coefficient and fractal dimension of rock fracture surfaces. Int J Rock Mech Min Sci. 2015;75(4):15–22. doi:10.1016/j.ijrmms.2015.01.007.
37. Zhao Z. On the heat transfer coefficient between rock fracture walls and flowing fluid. Comput Geotech. 2014;59:105–11. doi:10.1016/j.compgeo.2014.03.002.
38. Rong G, Tan J, Zhan H, He R, Zhang Z. Quantitative evaluation of fracture geometry influence on nonlinear flow in a single rock fracture. J Hydrol. 2020;589(1–2):125162. doi:10.1016/j.jhydrol.2020.125162.

39. Wang Z, Zhou C, Wang F, Li C, Xie H. Channeling flow and anomalous transport due to the complex void structure of rock fractures. J Hydrol. 2021;601(7):126624. doi:10.1016/j.jhydrol.2021.126624.
40. Cook NGW. Natural joints in rock: mechanical, hydraulic and seismic behaviour and properties under normal stress. Int J Rock Mech Min Sci Geomech Abstr. 1992;29(3):198–223. doi:10.1016/0148-9062(92)93656-5.